

Revisiting Lightweight Low-Light Image Enhancement: From a YUV Color Space Perspective

Hailong Yan^{1,2}, Shice Liu², Xiangtao Zhang¹,
Lujian Yao², Fengxiang Yang², Jinwei Chen², Bo Li^{2*}

¹UESTC ²vivo Mobile Communication Co. Ltd

Abstract

In the current era of mobile internet, Lightweight Low-Light Image Enhancement (L3IE) is critical for mobile devices, which faces a persistent trade-off between visual quality and model compactness. While recent methods employ disentangling strategies to simplify lightweight architectural design, such as Retinex theory and YUV color space transformations, their performance is fundamentally limited by overlooking channel-specific degradation patterns and cross-channel interactions. To address this gap, we perform a frequency-domain analysis that confirms the superiority of the YUV color space for L3IE. We identify a key insight: the Y channel primarily loses low-frequency content, while the UV channels are corrupted by high-frequency noise. Leveraging this finding, we propose a novel YUV-based paradigm that strategically restores channels using a Dual-Stream Global-Local Attention module for the Y channel, a Y-guided Local-Aware Frequency Attention module for the UV channels, and a Guided Interaction module for final feature fusion. Extensive experiments validate that our model establishes a new state-of-the-art on multiple benchmarks, delivering superior visual quality with a significantly lower parameter count.

Introduction

Lightweight Low-Light Image Enhancement (L3IE) aims to improve image quality under poor lighting conditions in real time on low-computing-power devices. With the increasing demand for mobile camera equipment such as drones and recorders, L3IE is becoming increasingly important.

Early L3IE methods, such as those relying on heuristic rules (Lee, Lee, and Kim 2013), often yielded limited enhancement quality. With the advent of deep learning, subsequent research efforts (Wei et al. 2018; Fu et al. 2023) began to leverage the modeling capabilities of deep networks to directly recover brightness from low-exposure RGB images. However, these methods consistently faced a challenging trade-off: lightweight models tended to produce sub-optimal results, while high-performance models were too computationally intensive to be considered truly lightweight.

Recently, a paradigm shift towards disentanglement-based modular designs has dominated L3IE research.

Retinex-based methods (Cai et al. 2023) are a representative class, which disentangle RGB images into illumination and reflectance components for separate processing. A significant drawback, however, is that achieving effective disentanglement often necessitates deeper or multi-branch architectures, thereby increasing computational complexity.

An alternative line of work involves methods based on the YUV color space transformation. Inspired by the human visual system where rod cells perceive luminance and cone cells perceive color, these methods process the luminance (Y) and chrominance (UV) channels independently. Despite their promise, most YUV-based methods suffer from two principal limitations. First, they often apply homogeneous processing to all channels, and overlook perceptual differences across channels (Guo and Hu 2023; Niu et al. 2025). Second, other methods (Wang et al. 2024a; Zhu et al. 2024) optimize the luminance and chrominance channels in isolation, failing to establish effective cross-channel interaction, which hinders joint optimization and overall performance.

In order to guide the design of a more effective yet lightweight model, our work begins with an in-depth analysis of RGB and YUV degradation characteristics under low-light conditions, leveraging frequency-domain analysis. As illustrated in Fig. 1, the RGB channels exhibit highly similar degradation trends, indicating strong inter-channel entanglement. This complicates the simultaneous tasks of brightness enhancement and noise suppression, which presents a significant challenge for efficient network design. In contrast, the YUV channels offer an inherent advantage by naturally disentangling these degradations. Specifically, in low-light scenarios, the Y channel primarily suffers from a loss of low-frequency energy and a minor increase in high-frequency noise, which visually manifests as diminished brightness. Conversely, the UV channels are predominantly corrupted by substantial high-frequency noise, while their low-frequency components remain relatively stable.

Based on the aforementioned observations, we propose a novel YUV-based L3IE paradigm designed to systematically address low- and high-frequency degradations in low-light images. Our architecture is composed of three specialized modules. Firstly, a Dual-Stream Global-Local Attention (DSGLA) module is introduced to process the Y channel, which comprises a Dilated-Depth Self Attention (DDSA) to capture long-range dependencies and a Ghost-Gated Ag-

*Corresponding author.

Copyright © 2026, Association for the Advancement of Artificial Intelligence (www.aaai.org). All rights reserved.

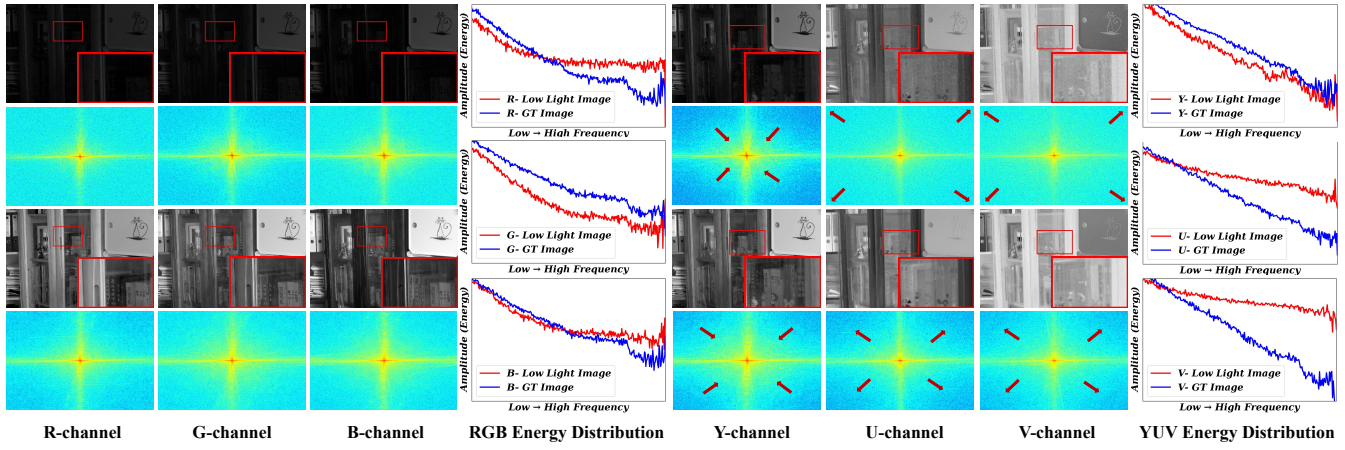


Figure 1: Comparison of degradation patterns across RGB and YUV color spaces under low-light conditions. The first two rows show the low-light input images and their corresponding frequency spectrums (via Fourier Transform), while the last two rows show the ground truth (GT) images and their spectrums. Unlike the RGB channel-entangled degradation, YUV channels exhibit clearer disentangled: the Y channel mainly shows low-frequency luminance degradation, accompanied by potential high-frequency noise, while the U/V channels contain more prominent high-frequency chrominance noise.

gregation (GGA) to enhance local detail awareness. This dual-stream design makes it possible to effectively model the global low-frequency structures and the local high-frequency details. Secondly, to address the high-frequency noise dominating the UV channels, we introduce a Local-Aware Frequency Attention (LAFA) module. The LAFA incorporates guidance from the enhanced Y-channel features, and leverages a Frequency Channel Attention (FCA) mechanism on Fourier features to improve denoising. Thirdly, a Guided Interaction (GI) module orchestrates the fusion of Y and UV features via cross-channel and frequency-aware interactions, yielding a coherently enhanced image.

In summary, our main contributions are:

- Through a comprehensive frequency-domain analysis of low-light degradation, we demonstrate that addressing the L3IE task within the YUV color space facilitates the design of more compact and effective models.
- We introduce a novel YUV-based L3IE paradigm featuring channel-specific processing for Y and UV, culminating in an effective fusion. Our 30K-parameter model sets a new benchmark for efficiency, requiring fewer parameters than even the most lightweight existing models.
- Extensive experiments show that our strategic design yields a model that achieves highly competitive performance against SOTA methods on all benchmarks.

Related Works

End-to-end RGB-based methods. These methods leverage the fitting capabilities of neural networks to directly process RGB images and produce brightness-enhanced results. (Lore, Akintayo, and Sarkar 2017) first adopted an autoencoder for joint denoising and brightening, followed by CNN-based methods (Zhang, Zhang, and Guo 2019; Guo et al. 2020; Yan et al. 2025a) that improved detail restoration through end-to-end or self-supervised learning. Considering CNNs are limited in modeling long-range dependencies,

Transformer-based approaches (Wang et al. 2023; Liu et al. 2024a) address this by leveraging global self-attention. (Xu et al. 2022) incorporated signal-to-noise priors for adaptive enhancement. In addition, diffusion-based methods (Wang et al. 2024c; Lv et al. 2024; Hou et al. 2023) have shown promising results in image quality and detail restoration. However, either transformers or diffusion models often suffer from high computational cost. In conclusion, end-to-end RGB-based methods face difficulties in effectively handling the complex interplay between brightness and noise.

Retinex-based L3IE. As a prominent disentanglement strategy for L3IE, Retinex-based L3IE (Zhao et al. 2021; Cai et al. 2023; Fu et al. 2023; Liu et al. 2024a; Yan, Huang, and Huang 2025; Liu et al. 2024b) disentangled an RGB image into reflectance and illumination for individual processing. These approaches theoretically allows robust structure preservation while modifying brightness. In practice, however, its efficacy is limited by two fundamental challenges. First, the Retinex decomposition itself is an ill-posed problem, since its simple priors like illumination smoothness frequently result in artifacts and unrealistic lighting. Second, stabilizing this ill-posed decomposition often demands complex, parameter-rich networks, directly contradicting the core objective of lightweight design.

YUV-based L3IE. The YUV color space offers a compelling alternative to Retinex, as its explicit separation of luminance and chrominance bypasses the ill-posed decomposition problem. This allows for a targeted brightness adjustment while preserving color fidelity (Guo and Hu 2023; Zhang et al. 2021; Niu et al. 2025). However, the promise of this approach is frequently unrealized as current methods are hampered by two critical flaws. First, they often employ channel-agnostic designs, applying uniform operations to Y and UV channels despite their distinct degradation patterns. Second, many recent works (Wang et al. 2024a; Zhu et al. 2024; Wang et al. 2024b; Brateanu et al. 2025) treat the lu-

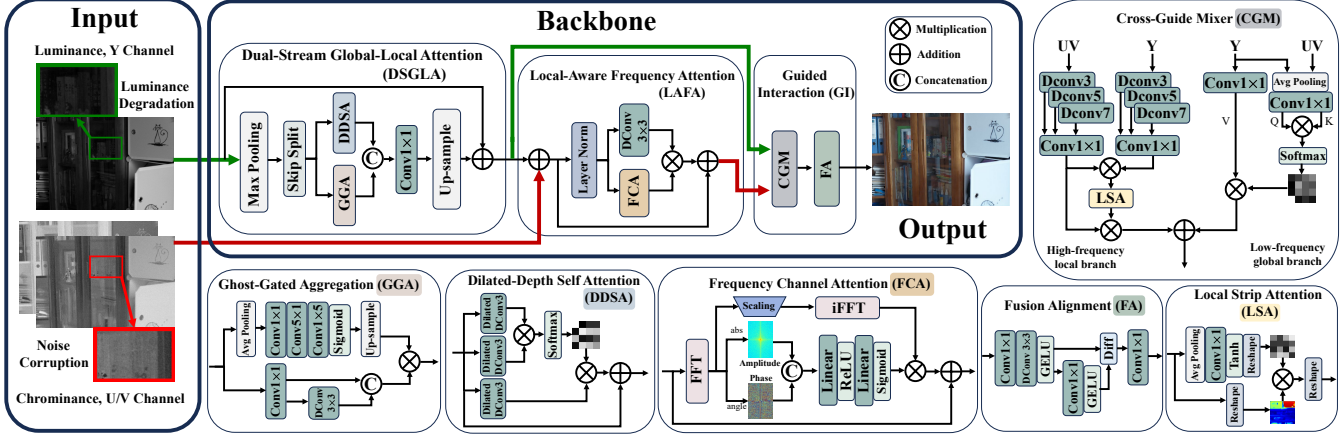


Figure 2: The overview of the proposed method. The Y channel is enhanced via DSGLA, while the UV channels are refined by LAFA with guidance from Y features. The GI module fuses luminance and chrominance features for consistent enhancement.

minance and chrominance pathways as isolated pipelines, lacking the sophisticated interaction necessary for coherent restoration. This oversight often leads to a suboptimal outcome, where enhancements in brightness come at the cost of color fidelity, or vice versa.

Proposed Method

Overall Pipeline

As shown in Fig. 2, the proposed framework consists of three modules: Dual-Stream Global-Local Attention (**DSGLA**), Local-Aware Frequency Attention (**LAFA**), and Guided Interaction (**GI**), corresponding to the luminance branch, chrominance branch, and cross-channel fusion. A low-light RGB image $I_{\text{low}}^{\text{RGB}} \in \mathbb{R}^{3 \times H \times W}$ is first converted to YUV color space. The **DSGLA** enhances the Y channel by addressing low-frequency luminance degradation via global-local attention, producing I_{enh}^Y . The **LAFA** takes I_{enh}^Y as guidance and the original UV input $I_{\text{low}}^{\text{UV}}$ to suppress high-frequency noise via frequency-aware attention, producing $I_{\text{enh}}^{\text{UV}}$. Finally, the **GI** fuses I_{enh}^Y and $I_{\text{enh}}^{\text{UV}}$ via cross-channel interaction, producing the final output $I_{\text{enh}}^{\text{RGB}}$.

DSGLA: Dual-Stream Global-Local Attention

Given that luminance degradation in the Y channel is generally global and low-frequency, while residual noise is local and high-frequency, the DSGLA module is designed to separately capture structural and detail cues. A max pooling operation is first applied to the Y-channel feature to emphasize dominant low-frequency structures and suppress irrelevant high-frequency noise, facilitating global context modeling and reducing computation in later stages.

Unlike (Brateanu et al. 2025) that processes the Y channel via a single pathway, DSGLA separates global structures and local details via a *channel-splitting* design. Specifically, the input feature $X \in \mathbb{R}^{C \times H \times W}$ is split along the channel dimension into two parts. X_{GI} is used for modeling global

structures and X_{Lo} focuses on refining local details.

$$X_{\text{GI}}, X_{\text{Lo}} = \text{Split}(X), \quad X_{\text{GI}}, X_{\text{Lo}} \in \mathbb{R}^{\frac{C}{2} \times H \times W}. \quad (1)$$

A. Global branch: Dilated-Depth Self Attention (DDSA)

To efficiently capture long-range dependencies in luminance features, the global branch adopts a self-attention mechanism enhanced by dilation and channel grouping. Specifically, given the input X_{GI} , we first apply a 1×1 pointwise convolution followed by a dilated depthwise convolution (DDConv) to generate the Q, K, and V features:

$$Q, K, V = \text{DDConv}_3(\text{Conv}_1(X_{\text{GI}})). \quad (2)$$

The dilated convolution expands the receptive field without increasing parameters, while depthwise and grouped operations reduce computational overhead, making the design both global-aware and efficient. The Q, K, and V tensors are reshaped and fed into a multi-head self-attention block:

$$\text{Attention}(Q, K, V) = \text{Softmax}(QK^\top / \sqrt{d})V, \quad (3)$$

where d is the dimensionality per head. The output of DDSA is referred to as F_{GI} . As self-attention excels at modeling global low-frequency dependencies, this branch is well-suited for capturing the large-scale luminance degradation in the Y channel, achieving enhanced structural sensitivity with reduced computational cost.

B. Local branch: Ghost-Gated Aggregation (GGA)

The Ghost-style structure efficiently reuses and enriches features, making it suitable for capturing fine-grained visual details with low computational cost (Han et al. 2020). Motivated by this, we design a **GGA** module that integrates the Ghost-style structure with a spatial gating mechanism to enhance local high-frequency representations.

While self-attention architectures are effective in modeling global dependencies and low-frequency semantics, convolutional operations excel at capturing high-frequency details (edges and textures), through local receptive fields (Li et al. 2025). Leveraging this property, the Ghost-style convolution further extends conventional convolutions by generating additional feature maps with fewer parameters, thus reducing redundancy and enriching feature diversity.

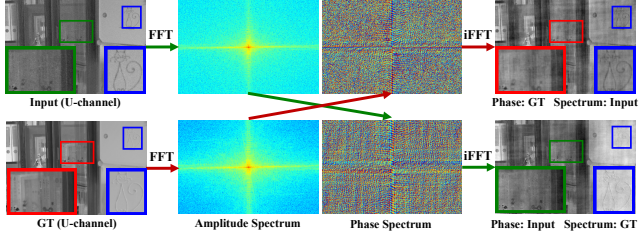


Figure 3: Visualization of spectrum swapping experiments.

First, the input feature $X_{\text{Lo}} \in \mathbb{R}^{C \times H \times W}$ is processed through two parallel branches to generate ghost features:

$$\begin{aligned} F_{\text{base}} &= \text{Conv}_1(X_{\text{Lo}}), \\ F_{\text{ghost}} &= \text{Concat}(F_{\text{base}}, \text{DConv}_3(F_{\text{base}})). \end{aligned} \quad (4)$$

Here, F_{base} represents the primary feature map, while the depthwise convolution (DConv) generates complementary features with fewer parameters. The concatenated output F_{ghost} encodes both efficiency and feature diversity.

Then, a spatial modulation map M is computed from a low-resolution shortcut pathway:

$$M = \text{Sigmoid}((\text{Up}(f_{\text{short}}(\text{AvgPool}(X_{\text{Lo}})))), \quad (5)$$

where $f_{\text{short}}(\cdot)$ consists of a series of grouped asymmetric convolutions (e.g., $1 \times 5, 5 \times 1$), $\text{Up}(\cdot)$ denotes upsample.

Finally, the output is modulated as: $F_{\text{Lo}} = F_{\text{ghost}} \odot M$.

The outputs of F_{Gl} and F_{Lo} from the DDSA and GGA modules are concatenated and passed through a 1×1 convolution for channel integration. This fusion combines global low-frequency structures and local high-frequency details, improving the representation for subsequent stages.

LAFA: Local-Aware Frequency Attention

In the UV channels, where degradation is dominated by high-frequency noise, frequency-domain modeling facilitates a more explicit disentanglement of signal and noise components. This not only promotes better distinguishing valid chrominance structures from interference, but also enhances its ability to suppress fine-grained degradation.

However, some frequency-domain methods (Qiao et al. 2023; Zhang et al. 2025a) focus exclusively on the amplitude spectrum, potentially overlooking the structural cues embedded in the phase. To assess the role of the phase, we conduct a spectrum replacement experiment, where only the amplitude is replaced by that of a GT image. The reconstruction preserves structural details consistent with the image providing the phase, as shown in the blue boxes (Fig. 3). This indicates that the phase spectrum aids structural alignment.

Therefore, we propose the LAFA to enhance the UV channels via luminance-guided frequency-domain modulation. Unlike previous methods that process UV features independently, LAFA incorporates the refined Y-channel features I_{enh}^Y from the DSGLA as structural priors. These features provide stable high-frequency guidance to help distinguish signals from high-frequency noise in chrominance.

Concretely, the LAFA takes the chrominance feature I_{low}^{UV} and the enhanced luminance feature I_{enh}^Y from DSGLA as

input. We first perform addition between I_{low}^{UV} and I_{enh}^Y to obtain a fused representation, which is transformed into the frequency domain: $X_A, X_P = \text{FFT}(I_{\text{low}}^{UV} + I_{\text{enh}}^Y)$, where X_A and X_P denote the amplitude and phase, respectively. We apply global average pooling to both components and concatenate them to form the spectral feature f .

$$f = \text{Concat}(\text{AvgPool}(X_A), \text{AvgPool}(X_P)). \quad (6)$$

And then, the features f are passed through a two-layer MLP to produce channel-wise attention weights W .

$$W = \text{Sigmoid}((\text{FC}_2(\text{ReLU}(\text{FC}_1(f)))). \quad (7)$$

In parallel, a learnable modulation mask $\hat{M} \in \mathbb{R}^{1 \times C \times 1 \times 1}$ is equipped to X_A, X_P to scale the spectrum. The spatial feature X' is recovered via the inverse FFT.

To further enhance local spatial consistency and suppress fine-grained chrominance noise, we apply a 3×3 depthwise convolution to the same fused input. The final output is obtained by element-wise multiplication of both branches:

$$X_{\text{LAFA}} = X' \cdot W \cdot \text{DConv}_3(I_{\text{low}}^{UV} + I_{\text{enh}}^Y) + (I_{\text{low}}^{UV} + I_{\text{enh}}^Y). \quad (8)$$

GI: Guided Interaction

For the purpose of achieving coordinated enhancement of structure and color, different from most YUV-based methods which process luminance and chrominance separately, we propose the Guided Interaction (GI) to explore the complementary potential of luminance and chrominance features. The GI consists of two sub-modules: the Cross-Guide Mixer (CGM) and the Fusion Alignment (FA) module.

The CGM consists of two branches. The global branch employs Transformer-style cross attention to refine low-frequency structures in the Y channel, guided by the relatively clean low-frequency cues from the UV features. This cross-channel interaction facilitates the restoration of degraded luminance. The local branch employs Local Strip Attention (LSA), which operates on horizontal strips rather than dense spatial correlations. Benefiting from the high-frequency details from the Y channel, LSA efficiently enhances fine-grained UV textures, ensuring that chrominance information is consistent with luminance details.

To guide UV refinement, we extract high-frequency components from both I_{enh}^Y and I_{low}^{UV} using multi-scale depthwise convolutions, denoted as $(F_{K:3}^Y, F_{K:5}^Y, F_{K:7}^Y)$ and $(F_{K:3}^{UV}, F_{K:5}^{UV}, F_{K:7}^{UV})$, respectively. These are concatenated as:

$$\begin{aligned} F_Y^{\text{high}} &= \text{Conv}_1(\text{Concat}(F_{K:3}^Y, F_{K:5}^Y, F_{K:7}^Y)), \\ F_{UV}^{\text{high}} &= \text{Conv}_1(\text{Concat}(F_{K:3}^{UV}, F_{K:5}^{UV}, F_{K:7}^{UV})). \end{aligned} \quad (9)$$

These are then fused by element-wise multiplication to form: $F = F_Y^{\text{high}} \cdot F_{UV}^{\text{high}}$, which is subsequently processed by the LSA module. LSA generates a channel-wise strip attention map by applying a 1×1 convolution followed by Tanh activation on pooled features, allowing attention to focus on horizontal strips and enhance fine-grained UV textures:

$$F_i^H = F_{UV}^{\text{high}} \cdot \sum_{i=1}^k P_i \cdot \text{Tanh}(\text{Conv}_1(\text{AvgPool}(F))_i), \quad (10)$$

Method	Venue	Category	Complexity		LOLv1			LOLv2-Real			LOLv2-Syn		
			Params \downarrow	FLOPs \downarrow	PSNR \uparrow	SSIM \uparrow	LPIPS \downarrow	PSNR \uparrow	SSIM \uparrow	LPIPS \downarrow	PSNR \uparrow	SSIM \uparrow	LPIPS \downarrow
Zero-DCE (Guo et al. 2020)	CVPR'20	RGB	0.075	4.83	21.880	0.640	0.335	16.059	0.580	0.313	17.712	0.815	0.169
SNR-Net (Xu et al. 2022)	CVPR'22	RGB	4.01	26.35	26.716	<u>0.851</u>	0.152	27.349	0.871	0.151	27.830	<u>0.942</u>	0.051
LPF (Dang, Zhong, and Wang 2023)	ICIP'23	RGB	0.082	4.83	25.659	0.848	0.133	28.015	0.879	0.166	28.159	0.939	0.062
LLFormer (Wang et al. 2023)	AAAI'23	RGB	24.55	22.52	26.106	0.830	0.166	29.307	0.866	0.141	27.574	0.936	0.065
UHDFour (Li et al. 2023b)	ICLR'23	RGB	15.90	57.42	26.308	0.836	0.143	27.472	0.878	0.162	27.087	0.912	0.078
FourierDiff (Lv et al. 2024)	CVPR'24	RGB	547.55	-	22.142	0.660	0.265	22.551	0.679	0.259	16.790	0.735	0.245
LIME (Guo, Li, and Ling 2016)	TIP'16	Retinex	-	-	18.947	0.448	0.408	18.495	0.469	0.402	18.391	0.773	0.218
RetinexFormer (Cai et al. 2023)	ICCV'23	Retinex	1.53	15.85	<u>27.140</u>	0.850	0.129	27.690	0.857	0.166	<u>29.024</u>	0.939	0.055
PairLIE (Fu et al. 2023)	CVPR'23	Retinex	0.33	20.81	23.526	0.755	0.248	24.026	0.803	0.227	21.681	0.820	0.224
CCNet (Jin, Wang, and Luo 2024)	TNNLS'24	LAB	3.78	-	26.665	0.842	0.156	27.963	0.878	0.149	27.982	0.935	0.058
CTNet (Xu et al. 2025)	PR'25	HSV	5.62	62.14	27.042	0.849	0.135	28.296	0.899	0.134	28.968	0.938	0.064
QuadPrior (Wang et al. 2024c)	CVPR'24	K-M	1252.75	1103.20	22.849	0.800	0.201	23.633	0.829	0.197	19.131	0.809	0.224
Bread (Guo and Hu 2023)	IJCV'23	YUV	2.02	19.85	25.299	0.847	0.155	26.916	0.883	0.152	19.379	0.810	0.243
Ghilie (Zhu et al. 2024)	TCSVT'24	YUV	3.05	199.36	25.182	0.840	0.155	28.584	0.880	0.126	24.627	0.905	0.104
END (Wang et al. 2024b)	TCSVT'24	YUV	7.91	270.44	26.364	0.850	0.133	<u>30.117</u>	<u>0.895</u>	<u>0.110</u>	28.738	0.939	<u>0.053</u>
LYTNet (Brateanu et al. 2025)	SPL'25	YUV	<u>0.045</u>	<u>1.70</u>	26.581	0.835	0.133	28.342	0.877	0.127	26.671	0.927	0.081
Ours		YUV	0.030	1.45	27.160	0.853	<u>0.131</u>	31.181	0.896	0.104	29.081	0.943	0.051

Table 1: Performance comparison of different L3IE models. The best results are in **bold**, and the second-best are underlined. The units for Param and FLOPs are M and G. Models above the line are large-scale, those below are lightweight.

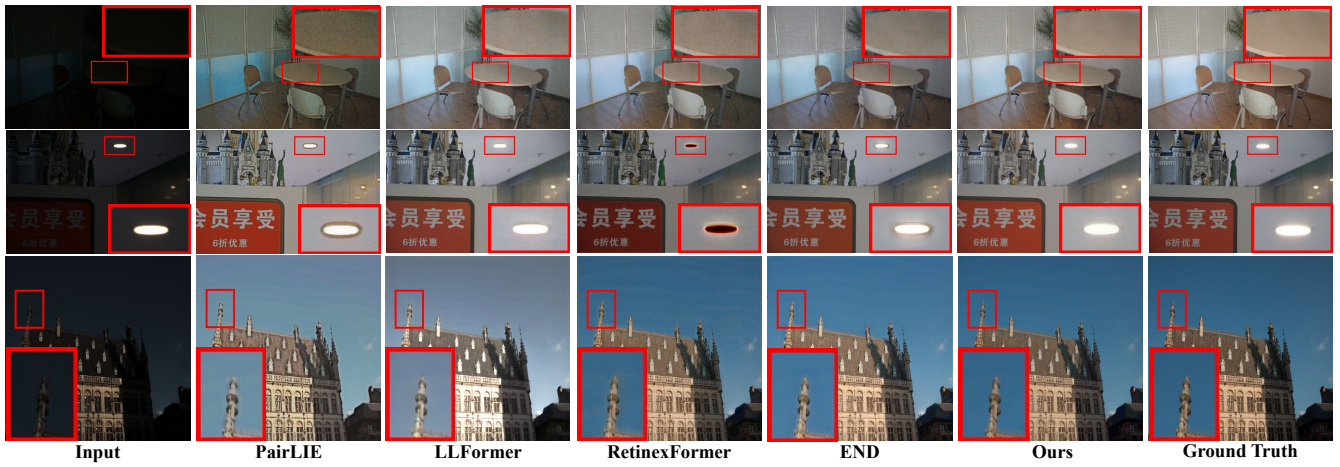


Figure 4: Visual comparison of L3IE methods on the LOL dataset. Red boxes highlight noise suppression.

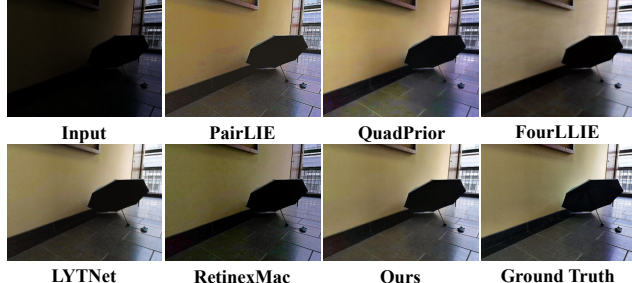


Figure 5: Visual comparison on LSRW.

where P_i denotes the unfolded horizontal patch at position i , and k is the kernel width. The output of CGM (F_{YUV}) is the sum of the global output F_g^L and the local output F_l^H :

$$F_{YUV} = F_g^L + F_l^H. \quad (11)$$

To ensure the consistency of luminance and chrominance information in the output, FA combines channel aggregation with offset removal to optimize the coordination of YUV channel features. Specifically, FA removes redundancy by

calculating the difference between features and activated features, avoiding inconsistencies between luminance and chrominance channels. This process can be expressed as:

$$\bar{F} = \text{GELU}(\text{DConv}_3(\text{Conv}_1(F_{YUV}))), \\ O = \bar{F} + \gamma \cdot (\bar{F} - \text{GELU}(\text{Conv}_1(\bar{F}))). \quad (12)$$

where \bar{F} is the refined feature, and γ is a learnable scaling factor. The final output O is the adjusted feature map that ensures the alignment of luminance and chrominance.

Experiments

Experimental Settings

Implementation Details. We implement our model on PyTorch and train it with the Adam optimizer ($\beta_1 = 0.9$, $\beta_2 = 0.999$) on an NVIDIA RTX 3090 GPU for 5,000 epochs, with an initial learning rate of 2×10^{-4} . During training, images are randomly cropped to 256×256 with a batch size of 1, and the network is optimized under the joint supervision of Smooth L1 and PSNR losses.

Datasets. To evaluate the effectiveness of our method, we conduct experiments on both paired and unpaired datasets.

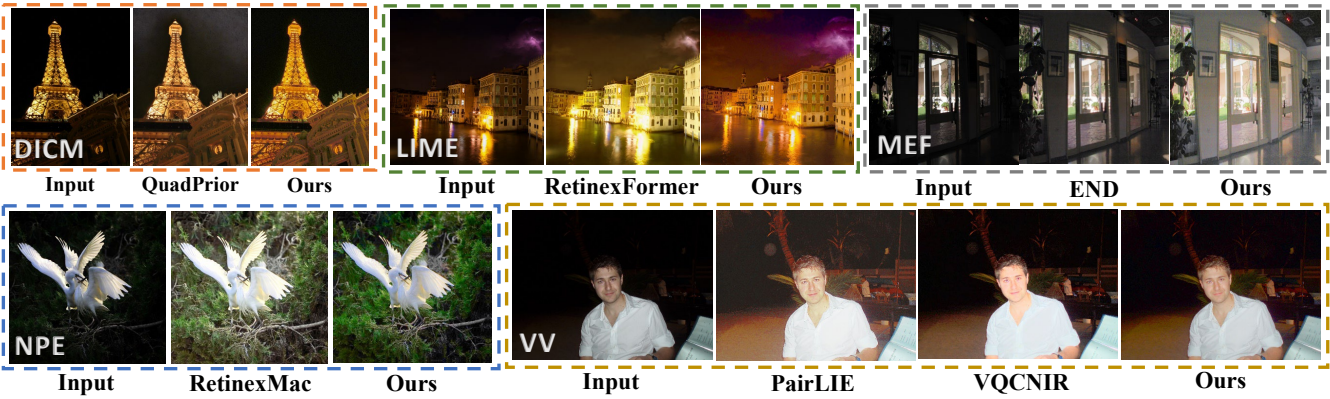


Figure 6: Visual comparison on unpaired datasets. Following RetinexFormer, one image per dataset is selected for comparison.

Method	Complexity		LSRW (Nikon)		LSRW (Huawei)	
	Params \downarrow	FLOPs \downarrow	PSNR \uparrow	SSIM \uparrow	PSNR \uparrow	SSIM \uparrow
Zero-DCE (Guo et al. 2020)	0.075	4.83	15.04	0.420	16.40	0.476
EnGAN (Jiang et al. 2021)	114.35	61.01	14.63	0.398	17.46	0.498
SNR-Net (Xu et al. 2022)	4.01	26.35	16.63	0.505	20.40	0.617
PairLIE (Fu et al. 2023)	0.33	20.81	15.52	0.435	18.99	0.563
FourLLIE (Wang, Wu, and Jin 2023)	1.49	16.29	<u>17.82</u>	0.504	21.11	0.626
RetinexFormer (Cai et al. 2023)	1.53	15.85	17.64	0.508	21.23	0.631
WaveMamba (Zou et al. 2024a)	1.52	15.97	17.34	0.519	21.19	0.639
QuadPrior (Wang et al. 2024c)	1252.75	1103.20	14.84	0.487	18.31	0.600
RetinexMac (Liu et al. 2024a)	2.29	29.59	16.66	0.461	19.07	0.596
DMFourLLIE (Zhang et al. 2024)	0.97	8.36	17.04	0.529	21.47	0.633
LYTNet (Brateam et al. 2025)	0.045	<u>1.70</u>	17.69	0.513	21.06	0.627
DarkIR (Feijoo et al. 2025)	3.32	7.25	16.12	0.507	20.78	0.625
CWNet (Zhang et al. 2025b)	1.23	11.30	-	-	21.51	0.640
Ours	0.03	1.45	17.99	<u>0.525</u>	21.52	0.642

Table 2: Performance comparison on the LSRW dataset. Best values are in **bold**, second-best are underlined.

The paired datasets include LOLv1 (Wei et al. 2018), LOLv2 (Yang et al. 2020), and LSRW (Hai et al. 2023). For unpaired evaluation, we utilize the DICM (Lee, Lee, and Kim 2013), LIME (Guo, Li, and Ling 2016), MEF (Ma, Zeng, and Wang 2015), NPE (Wang et al. 2013), and VV.

Metrics. Consistent with prior work, we evaluate our model using six key metrics to ensure a comprehensive assessment. We assess restoration quality on paired data using PSNR for pixel-wise fidelity, SSIM for structural similarity, and the perceptual metric LPIPS (Zhang et al. 2018), which captures perceptual differences more effectively than pixel-based metrics. Model efficiency is measured via Parameters (Params) and FLOPs, which indicate the model’s memory usage and computational cost, respectively. Additionally, the non-reference metric NIQE (Mittal et al. 2012) is employed specifically for quality assessment on unpaired datasets.

Quantitative and Visual Comparisons

Results on Pair Datasets. As shown in Tables 1 and 2, our method performs excellently on both LOL and LSRW. On LOL, we achieve the highest average PSNR of 29.141 dB and the second-lowest LPIPS of 0.095, while on LSRW, we obtain PSNRs of 17.99 dB and 21.52 dB, and SSIMs of 0.525 and 0.642, respectively. Using only 0.03M parameters and 1.45 GFLOPs, our method balances performance and efficiency. Compared to larger models like RetinexFormer (1.53M parameters, 15.85 GFLOPs), it reduces computational cost while maintaining quality. Compared to smaller

models like LYTNet (0.045M parameters, 1.70 GFLOPs), our method outperforms them in both datasets, showing a clear advantage in performance and efficiency.

Method	Params \downarrow	FLOPs \downarrow	DICM	LIME	MEF	NPE	VV	Average \downarrow
Zero-DCE (Guo et al. 2020)	0.075	4.83	3.535	<u>4.271</u>	3.680	4.048	3.927	3.892
RetinexDIP (Zhai et al. 2021)	0.71	-	3.383	<u>3.741</u>	3.669	4.947	3.975	3.943
SNR-Net (Xu et al. 2022)	4.01	26.35	3.586	<u>5.844</u>	4.060	4.700	5.589	4.756
Bread (Guo and Hu 2023)	2.02	19.85	3.737	4.528	4.229	4.293	3.596	4.077
PairLIE (Fu et al. 2023)	0.33	20.81	4.120	4.516	4.176	4.358	3.662	4.116
Retinexformer (Cai et al. 2023)	1.53	15.85	3.651	4.276	4.230	4.381	3.981	4.104
GSAD (He et al. 2023)	17.43	-	3.902	<u>4.547</u>	4.339	4.736	4.051	4.215
SWANet (He et al. 2023)	6.86	55.40	<u>3.169</u>	4.786	4.100	4.121	3.335	3.902
VQCNIR (Zou et al. 2024b)	45.93	162.46	3.961	4.103	4.680	4.258	3.346	4.070
RetinexMac (Liu et al. 2024a)	2.29	29.59	3.064	4.191	<u>3.613</u>	3.777	<u>3.201</u>	3.569
Ours	0.030	1.45	3.623	3.594	<u>3.334</u>	4.071	<u>3.126</u>	3.550

Table 3: NIQE comparison on five unpair datasets. Best values are in **bold**, second-best are underlined.

Fig. 4 and 5 show the visual comparisons on the LOL (Wei et al. 2018; Yang et al. 2020) and LSRW (Hai et al. 2023) datasets. Our method enhances brightness while preserving dark region details, achieving more balanced and natural results. Unlike methods like LLFormer (Wang et al. 2023), which struggle with uniform brightness, our approach avoids overexposure and effectively improves low-light areas. It also suppresses noise in dark regions better than methods like LLFormer (Wang et al. 2023), producing cleaner, less grainy images. Additionally, our method maintains natural color balance, whereas other methods, such as RetinexMac (Liu et al. 2024a), introduce color shifts, leading to more realistic and visually pleasing results.

Results on Unpair Datasets. As shown in Table 3, our method achieves an average NIQE score of 3.550 across five unpaired datasets, outperforming RetinexMac and VQCNIR. It achieves the lowest NIQE scores on DICM (3.535) and MEF (3.334), indicating superior image quality.

In Fig. 6, our method enhances brightness, preserves fine details, and effectively reduces noise, especially in low-light areas. Compared to QuadPrior, it also maintains more natural color, resulting in clearer and more realistic images.

Ablation Studies and Analyses

Replacing YUV with RGB. We conducted a critical ablation study to empirically prove the superiority of the YUV color space over RGB for L3IE using our proposed archi-

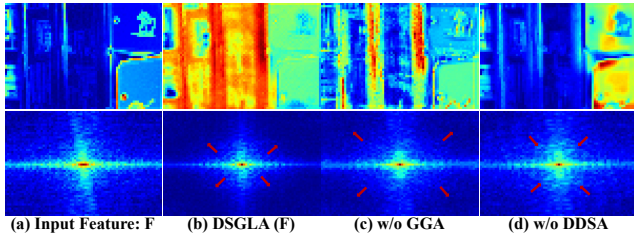


Figure 7: Feature Spectrum Visualization of DSGLA.

Color	R-GB	G-RB	B-GR	Y-UV
PSNR \uparrow	26.65	26.69	26.35	27.16
SSIM \uparrow	0.841	0.847	0.842	0.853
LPIPS \downarrow	0.152	<u>0.141</u>	0.148	0.131

Table 4: Ablation study on Table 5: Ablation study on different color space. Table 5: Ablation study on downsampling ratios.

ture. As shown in Table 4, we evaluated several RGB input configurations against our standard YUV input. The results are decisive: the YUV-based model significantly outperforms all RGB counterparts on all metrics. The G-RB configuration emerged as the best-performing RGB variant, a result consistent with the spectral similarity between the G and Y channels (Fig. 1). This experiment provides compelling evidence that the performance gains of our model stem directly from the strategic advantages of channel-specific processing in the YUV space.

Method	PSNR \uparrow	SSIM \uparrow	LPIPS \downarrow	LOE \downarrow	MAE \downarrow
w/o DSGLA	26.502	0.831	0.163	0.269	0.092
w/o DDSA	26.643	0.845	0.138	<u>0.255</u>	0.086
w/o GGA	26.767	0.849	0.134	0.262	<u>0.084</u>
HFERB (Li et al. 2023a)	26.725	0.849	<u>0.133</u>	0.260	0.090
A-MSA (Wang et al. 2023)	26.555	0.842	0.139	0.262	0.098
DHSA (Sun et al. 2024)	26.908	0.846	0.134	0.258	0.094
Ours	27.160	0.853	0.131	0.254	0.081

Table 6: Quantitative Results of DSGLA Ablation Study.

Analysis of DSGLA. To verify the effectiveness of DSGLA, we conduct ablation experiments on its submodules, with results shown in Table 6 and Fig. 7.

Removing DSGLA causes a clear performance drop. Further, removing DDSA (PSNR:-0.517dB) weakens global structure modeling, while removing GGA (PSNR:-0.393dB) degrades local texture restoration. Our method also outperforms recent attention designs like DHSA.

We also analyze the impact of downsampling ratios (Table 5). The best performance is achieved with an 8x. Since the Y degradation mainly affects low-frequency luminance across the image, capturing the overall brightness distribution is crucial. MaxPooling allows for effective spatial compression while preserving essential structures and suppressing noise in low-contrast regions. A small ratio (2 or 4) fails to capture global luminance trends, while a large ratio (16) loses too much spatial detail, impairing texture recovery.

In Fig.7(b), DSGLA effectively enhances high-frequency details and suppresses low-frequency degradation, aligning with the Y channel’s dominant low-frequency luminance interference. Without GGA, high-frequency texture responses

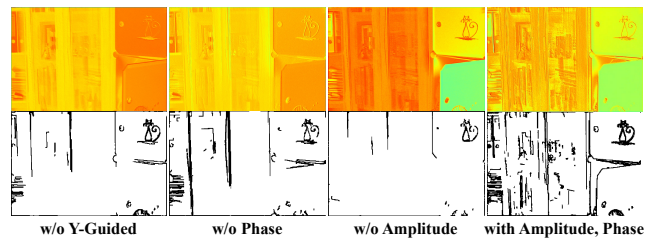


Figure 8: Visual of LAFA Effects on Feature Representation. Each block shows the LAFA output feature and the Canny edge of (output-input) feature difference (bottom-right).

are notably weakened; without DDSA, low-frequency information is insufficiently modeled.

Method	PSNR \uparrow	SSIM \uparrow	LPIPS \downarrow	LOE \downarrow
w/o LAFA	26.551	0.833	0.175	0.263
w/o Phase	26.748	0.841	0.149	0.263
w/o Amplitude	26.624	0.838	0.158	<u>0.255</u>
w/o Y-Guided	26.426	0.838	0.155	0.261
MCSF (Cui et al. 2023)	26.872	<u>0.850</u>	<u>0.135</u>	0.259
EB (Feijoo et al. 2025)	26.926	0.853	0.136	0.255
Ours	27.160	0.853	0.131	0.254

Table 7: Quantitative Results of LAFA Ablation Study.

Analysis of LAFA. We perform ablation studies to evaluate LAFA. As shown in Table 7, removing amplitude weakens noise suppression, while omitting phase or Y-guided reduces structural consistency and detail alignment.

Fig. 8 presents the visual comparisons. Without amplitude, fine textures are lost and noise remains in flat regions. Without phase, edge structures become blurry and disconnected. Removing Y-guidance causes inconsistencies in structure across channels. In contrast, using all components results in sharper, more coherent edge representations.

Method	PSNR \uparrow	SSIM \uparrow	LPIPS \downarrow	LOE \downarrow	MAE \downarrow
Concatenation	26.070	0.814	0.191	0.268	0.092
Sum	25.997	0.834	0.158	0.260	0.093
w/o FA	26.467	0.839	0.142	0.259	0.095
HFB (Li et al. 2025)	<u>26.725</u>	0.850	<u>0.133</u>	0.260	0.086
LCA (Yan et al. 2025b)	26.627	<u>0.851</u>	0.137	<u>0.255</u>	0.089
Ours	27.160	0.853	0.131	0.254	0.081

Table 8: Quantitative Results of GI Ablation Study.

Analysis of GI. To evaluate the GI, we compare it with conventional fusion strategies (concat, sum) and recent fusion designs. As shown in Table 8, naive fusion methods perform poorly due to their inability to fully leverage the complementary roles of the Y and UV channels. In contrast, GI achieves consistently better scores, highlighting its advantage in modeling cross-channel dependencies.

We further analyze the GI via frequency-domain visualizations, as shown in Fig. 9. In the CGM, the local branch uses Y features to guide high-frequency enhancement in the UV channels, while the global branch leverages UV cues to refine low-frequency structures in the Y channel. This bidirectional guidance aligns structural and chromatic features

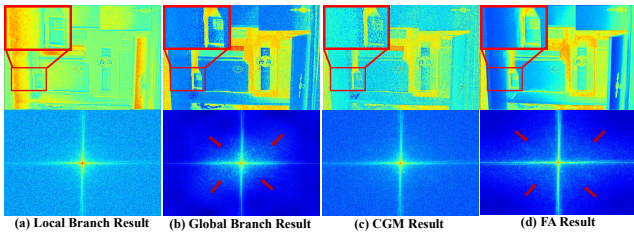


Figure 9: Feature Spectrum Visualization of GI.

across channels. The subsequent FA module suppresses redundant high-frequency noise and strengthens dominant low-frequency components, leading to sharper structural contours and more consistent color transitions.

Latency Performance Evaluation. Table 9 shows latency results on both GPU and CPU platforms. Our model achieves a latency of **6.5 ms** on GPU and **124.1 ms** on CPU, outperforming RetinexMac (32.4/739.3 ms) and LYTNet (7.9/165.8 ms). With only 30K parameters and 1.45 GFLOPs, it ensures efficient real-time processing on both high-performance and resource-constrained devices.

In contrast, other models with higher latency and larger parameters perform poorly in such environments. Our method offers a significant advantage in low-latency, efficient processing across different hardware platforms.

Method	RetinexMac	END	RetinexFormer	LYTNet	Ours
Latency (ms)	32.4/739.3	92.7/-	18.9/382.5	7.9/165.8	6.5/124.1
Params (M)	2.29	7.91	1.53	<u>0.05</u>	0.03

Table 9: Latency comparison on both GPU/CPU platforms.

Limitations. Our work validates a YUV-based framework, but its optimality relative to other color spaces remains an open question. We believe exploring alternative color representations is a promising avenue for future L3IE research to achieve even greater performance.

Conclusion

This paper revisits the lightweight low-light image enhancement (L3IE) task from the color space perspective and introduces a novel YUV-based approach. The proposed framework concludes three modules: DSGLA capturing global-local structures in the Y channel, LAFA suppressing high-frequency noise in the UV channel via illumination-guided frequency-aware modulation, and GI enabling structure-aware fusion between Y and UV. With only 30K parameters, our proposed framework not only outperforms other SOTA L3IE methods in low-light enhancement but also achieves an excellent balance between visual quality and model compactness across multiple benchmarks.

References

Brateanu, A.; Balmez, R.; Avram, A.; Orhei, C.; and Ancauti, C. 2025. Lyt-net: Lightweight yuv transformer-based network for low-light image enhancement. *IEEE SPL*.

Cai, Y.; Bian, H.; Lin, J.; Wang, H.; Timofte, R.; and Zhang, Y. 2023. Retinexformer: One-stage retinex-based trans-

former for low-light image enhancement. In *ICCV*, 12504–12513.

Cui, Y.; Ren, W.; Cao, X.; and Knoll, A. 2023. Image restoration via frequency selection. *IEEE TPAMI*, 46(2): 1093–1108.

Dang, J.-c.; Zhong, Y.; and Wang, L.-s. 2023. You only need 80k parameters to enhance image: learning periodic features for image enhancement. In *ICIP*, 885–889. IEEE.

Feijoo, D.; Benito, J. C.; Garcia, A.; and Conde, M. V. 2025. Darkir: Robust low-light image restoration. In *CVPR*, 10879–10889.

Fu, Z.; Yang, Y.; Tu, X.; Huang, Y.; Ding, X.; and Ma, K.-K. 2023. Learning a simple low-light image enhancer from paired low-light instances. In *CVPR*, 22252–22261.

Guo, C.; Li, C.; Guo, J.; Loy, C. C.; Hou, J.; Kwong, S.; and Cong, R. 2020. Zero-reference deep curve estimation for low-light image enhancement. In *CVPR*, 1780–1789.

Guo, X.; and Hu, Q. 2023. Low-light image enhancement via breaking down the darkness. *IJCV*, 131(1): 48–66.

Guo, X.; Li, Y.; and Ling, H. 2016. LIME: Low-light image enhancement via illumination map estimation. *IEEE TIP*, 26(2): 982–993.

Hai, J.; Xuan, Z.; Yang, R.; Hao, Y.; Zou, F.; Lin, F.; and Han, S. 2023. R2net: Low-light image enhancement via real-low to real-normal network. *JVCIR*, 90: 103712.

Han, K.; Wang, Y.; Tian, Q.; Guo, J.; Xu, C.; and Xu, C. 2020. Ghostnet: More features from cheap operations. In *CVPR*, 1580–1589.

He, Z.; Ran, W.; Liu, S.; Li, K.; Lu, J.; Xie, C.; Liu, Y.; and Lu, H. 2023. Low-light image enhancement with multi-scale attention and frequency-domain optimization. *IEEE TCSV*, 34(4): 2861–2875.

Hou, J.; Zhu, Z.; Hou, J.; Liu, H.; Zeng, H.; and Yuan, H. 2023. Global structure-aware diffusion process for low-light image enhancement. *NeurIPS*, 36: 79734–79747.

Jiang, Y.; Gong, X.; Liu, D.; Cheng, Y.; Fang, C.; Shen, X.; Yang, J.; Zhou, P.; and Wang, Z. 2021. Enlightengan: Deep light enhancement without paired supervision. *IEEE TIP*, 30: 2340–2349.

Jin, Z.; Wang, C.; and Luo, X. 2024. Colorization-inspired customized low-light image enhancement by a decoupled network. *IEEE TNNLS*.

Lee, C.; Lee, C.; and Kim, C.-S. 2013. Contrast enhancement based on layered difference representation of 2D histograms. *IEEE TIP*, 22(12): 5372–5384.

Li, A.; Zhang, L.; Liu, Y.; and Zhu, C. 2023a. Feature modulation transformer: Cross-refinement of global representation via high-frequency prior for image super-resolution. In *ICCV*, 12514–12524.

Li, A.; Zhang, L.; Liu, Y.; and Zhu, C. 2025. Exploring frequency-inspired optimization in transformer for efficient single image super-resolution. *IEEE TPAMI*.

Li, C.; Guo, C.-L.; Zhou, M.; Liang, Z.; Zhou, S.; Feng, R.; and Loy, C. C. 2023b. EmbeddingFourier for Ultra-High-Definition Low-Light Image Enhancement. In *ICLR*.

Liu, C.; Wang, Z.; Birch, P.; and Wang, X. 2024a. Efficient retinex-based framework for low-light image enhancement without additional networks. *IEEE TCSVT*.

Liu, X.; Wu, Z.; Li, A.; Vasluiianu, F.-A.; Zhang, Y.; Gu, S.; Zhang, L.; Zhu, C.; Timofte, R.; Jin, Z.; et al. 2024b. NTIRE 2024 challenge on low light image enhancement: Methods and results. In *CVPRW*, 6571–6594.

Lore, K. G.; Akintayo, A.; and Sarkar, S. 2017. LLNet: A deep autoencoder approach to natural low-light image enhancement. *Pattern Recognition*, 61: 650–662.

Lv, X.; Zhang, S.; Wang, C.; Zheng, Y.; Zhong, B.; Li, C.; and Nie, L. 2024. Fourier priors-guided diffusion for zero-shot joint low-light enhancement and deblurring. In *CVPR*, 25378–25388.

Ma, K.; Zeng, K.; and Wang, Z. 2015. Perceptual quality assessment for multi-exposure image fusion. *IEEE TIP*, 24(11): 3345–3356.

Mittal, A.; Soundararajan, R.; Bovik, A. C.; and et. al. 2012. Making a “completely blind” image quality analyzer. *IEEE SPL*, 20(3): 209–212.

Niu, Y.; Li, F.; Li, Y.; Chen, S.; and Chen, Y. 2025. Adaptive Luminance Enhancement and High-Fidelity Color Correction for Low-Light Image Enhancement. *IEEE TCI*.

Qiao, Y.; Shao, M.; Wang, L.; and Zuo, W. 2023. Learning depth-density priors for Fourier-based unpaired image restoration. *IEEE TCSVT*, 34(4): 2604–2618.

Sun, S.; Ren, W.; Gao, X.; Wang, R.; and Cao, X. 2024. Restoring images in adverse weather conditions via histogram transformer. In *ECCV*, 111–129. Springer.

Wang, C.; Wu, H.; and Jin, Z. 2023. Fourllie: Boosting low-light image enhancement by fourier frequency information. In *ACM MM*, 7459–7469.

Wang, H.; Yan, X.; Hou, X.; Li, J.; Dun, Y.; and Zhang, K. 2024a. Division gets better: Learning brightness-aware and detail-sensitive representations for low-light image enhancement. *Knowledge-Based Systems*, 299: 111958.

Wang, H.; Yan, X.; Hou, X.; Zhang, K.; and Dun, Y. 2024b. Extracting noise and darkness: Low-light image enhancement via dual prior guidance. *IEEE TCSVT*.

Wang, S.; Zheng, J.; Hu, H.-M.; and Li, B. 2013. Naturalness preserved enhancement algorithm for non-uniform illumination images. *IEEE TIP*, 22(9): 3538–3548.

Wang, T.; Zhang, K.; Shen, T.; Luo, W.; Stenger, B.; and Lu, T. 2023. Ultra-high-definition low-light image enhancement: A benchmark and transformer-based method. In *AAAI*, volume 37, 2654–2662.

Wang, W.; Yang, H.; Fu, J.; and Liu, J. 2024c. Zero-reference low-light enhancement via physical quadruple priors. In *CVPR*, 26057–26066.

Wei, C.; Wang, W.; Yang, W.; and Liu, J. 2018. Deep retinex decomposition for low-light enhancement. *arXiv preprint arXiv:1808.04560*.

Xie, L.; Cong, R.; Dai, J.; Yang, W.; Pan, J.; and Wu, H. 2025. CTNet: Color transformation network for low-light image enhancement. *PR*, 112360.

Xu, X.; Wang, R.; Fu, C.-W.; and Jia, J. 2022. Snr-aware low-light image enhancement. In *CVPR*, 17714–17724.

Yan, H.; Huang, J.; and Huang, T. 2025. IGDNet: Zero-Shot Robust Underexposed Image Enhancement via Illumination-Guided and Denoising. *arXiv preprint arXiv:2507.02445*.

Yan, H.; Li, A.; Zhang, X.; Liu, Z.; Shi, Z.; Zhu, C.; and Zhang, L. 2025a. MobileIE: An Extremely Lightweight and Effective ConvNet for Real-Time Image Enhancement on Mobile Devices. In *ICCV*.

Yan, Q.; Feng, Y.; Zhang, C.; Pang, G.; Shi, K.; Wu, P.; Dong, W.; Sun, J.; and Zhang, Y. 2025b. Hvi: A new color space for low-light image enhancement. In *CVPR*, 5678–5687.

Yang, W.; Wang, S.; Fang, Y.; Wang, Y.; and Liu, J. 2020. From fidelity to perceptual quality: A semi-supervised approach for low-light image enhancement. In *CVPR*, 3063–3072.

Zhang, J.; Wang, X.; Li, Y.; and Wang, W. 2025a. PRNet: Low-Light Image Enhancement Based on Fourier Transform. *IEEE TIM*.

Zhang, R.; Isola, P.; Efros, A. A.; Shechtman, E.; and Wang, O. 2018. The unreasonable effectiveness of deep features as a perceptual metric. In *CVPR*, 586–595.

Zhang, T.; Liu, P.; Lu, Y.; Cai, M.; Zhang, Z.; Zhang, Z.; and Zhou, Q. 2025b. Cwnet: Causal wavelet network for low-light image enhancement. In *ICCV*, 8789–8799.

Zhang, T.; Liu, P.; Zhao, M.; and Lv, H. 2024. DMFourL-LIE: dual-stage and multi-branch fourier network for low-light image enhancement. In *Proceedings of the 32nd ACM International Conference on Multimedia*, 7434–7443.

Zhang, Y.; Di, X.; Zhang, B.; Ji, R.; and Wang, C. 2021. Better than reference in low-light image enhancement: Conditional re-enhancement network. *IEEE TIP*, 31: 759–772.

Zhang, Y.; Zhang, J.; and Guo, X. 2019. Kindling the darkness: A practical low-light image enhancer. In *ACM MM*, 1632–1640.

Zhao, Z.; Xiong, B.; Wang, L.; Ou, Q.; Yu, L.; and Kuang, F. 2021. RetinexDIP: A unified deep framework for low-light image enhancement. *IEEE TCSVT*, 32(3): 1076–1088.

Zhu, Z.; Yang, X.; Lu, R.; Shen, T.; Zhang, T.; and Wang, S. 2024. Ghost imaging in the dark: A multi-illumination estimation network for low-light image enhancement. *IEEE TCSVT*.

Zou, W.; Gao, H.; Yang, W.; and Liu, T. 2024a. Wavemamba: Wavelet state space model for ultra-high-definition low-light image enhancement. In *ACM MM*, 1534–1543.

Zou, W.; Gao, H.; Ye, T.; Chen, L.; Yang, W.; Huang, S.; Chen, H.; and Chen, S. 2024b. VQCNIR: clearer night image restoration with vector-quantized codebook. In *AAAI*, volume 38, 7873–7881.